Climate-informed Flood Risk Mapping using a GAN-based Approach (ExGAN)

Rafia Belhajjam[1], Abdelaziz Chaqdid[2], Naji Yebari[1],
Mohammed Seaid[3] and Nabil El Moçayd[4,*]

[1] Faculté des sciences, University Abdelmalek Essaadi, Tetouan, Morocco

[2] Institute of Applied Physics, University Mohammed VI Polytechnic, Benguerir, Morocco

[3] Department of Engineering, University of Durham, South Road, DH1 3LE, United Kingdom

[4] College of Agriculture and Environmental Sciences, University Mohammed VI Polytechnic, Benguerir, Morocco

[*] Correspondence to: Nabil El Moçayd (nabil.elmocayd@um6p.ma)

Abstract

This study develops a class of robust models for flood risk mapping in highly vulnerable regions by focusing on accurately depicting extreme precipitation patterns aligned with regional climates. By implementing sophisticated hydrodynamics modeling and advanced probabilistic approaches, the present work underscores the efficacy of physical-based methodologies in the flood risk assessment. We propose a machine learning based ExGAN to address the challenge of synthesizing extreme precipitation scenarios which faithfully capture the nuances of local climatology. It is expected that through refined temporal disaggregation, the ExGAN approach exhibits exceptional proficiency in replicating a diverse spectrum of extreme precipitation patterns specific to the vulnerable region under scrutiny. Therefore, using these synthesized scenarios as inputs in a meticulously calibrated hydrological model would enable a comprehensive and detailed flood risk mapping exercise. To demonstrate the robustness of the developed mode, we perform a rigorous testing and validation within the highly susceptible Martil river basin, situated in the northern Mediterranean region of Morocco. The obtained results confirm that extending return periods would provide invaluable insights into the expanding geographical expanse of at-risk areas, clarifying the evolving landscape of vulnerability rather than merely amplifying inherent risk levels. Comparisons against the conventional Monte-Carlo sampling are also carried out in this study and the obtained results highlight significant overestimations within the latter, emphasizing the imperative need to account for diverse uncertainties beyond the basic sampling strategies within the realm of hydrodynamic modeling.

Keywords: Flood risk mapping, Climate-informed modeling, Hydrodynamics simulation, ExGAN, Extreme precipitation

1 Introduction

Climate-driven natural hazards are increasingly affecting populations worldwide and this situation is expected to exacerbate with the impacts of climate change (Mora et al., 2018). Among various natural disasters, flooding stands out as a recurrent and major concern in many regions even in water-stressed countries (Radwan et al., 2019; Satour et al., 2021). Therefore, developing reliable and realistic flood risk maps is of paramount importance. In practice, accurate flood risk mapping serves multiple purposes in engineering applications. Firstly, it empowers stakeholders to construct effective flood defenses, enact appropriate land use regulations, and establish early warning systems. In addition, by identifying high-risk areas, it facilitates strategic infrastructure planning, minimizing potential flood-related damages. Lastly, pinpointing flood-prone zones and natural floodplains enables policymakers to prioritize the conservation and restoration of ecosystems that offer crucial flood regulation services. Considerable efforts have been dedicated to this purpose, with the literature providing several tools for flood risk mapping. These tools encompass historical disaster assessment (Li et al., 2023), index system assessment (Satour et al., 2023), remote sensing impact assessment (Dash and Sar, 2020), and scenario simulation assessment (Neal et al., 2013). On the other hand, while each method has its own advantages and drawbacks, scenario simulation assessments are particularly appealing due to their ability to generate realistic flood maps. In fact these procedures rely on physically based hydrodynamics modeling, enabling the translation of entire hydrograph dynamics over watersheds. However, these methods face major challenges in the modeling stage such as generating multiple flooding scenarios that represent a major hurdle within this context. Although multiple factors contribute to flooding, extreme precipitation remains a key trigger (Ballesteros-Cánovas et al., 2015; Gai et al., 2018). Understanding and modeling these events have been a long-standing and significant challenge over the past decade. Numerical tools designed for flood risk mapping require a substantial amount of extreme precipitation scenarios to be reliable and yet, historical precipitation time series for specific stations usually provide only a limited number of extreme past events. From a statistical perspective, an extreme event is one with a close-to-zero probability of occurrence, often defined as the inverse of a defined return period (as long as possible). To address data scarcity, many Weather Generators (WGs) have been introduced to generate synthetic precipitation series enabling more accurate flood risk mappings.

The literature offers a comprehensive set of methods to build WGs, see for example (Ullrich et al., 2021) for an approach considering precipitation as a realization of the stochastic time process. This methodology involves simulating the occurrence of wet/dry days first, followed by assuming the intensity of precipitation follows a specific probability distribution. These statistics are inferred from observations from a single gauge. For instance, Richardson (1981) utilizes a Markov chain-based model to simulate wet/dry days whereas the precipitation intensity is simulated using an exponential distribution. The study demonstrates that this model reproduces precipitation seasonality with high confidence. This concept was further generalized by employing empirical distribution functions instead of the Markov chain model, as reported in Racsko et al. (1991). According to Semenov et al. (1998), this approach enhanced the accuracy of certain characteristics of the precipitation pattern, although spatial patterns were not considered. To overcome these limitations, statistics were inferred from multiple rain stations, employing different classes of statistical models. This included the use of hidden Markov Chain models (Hughes et al., 1999) or copula-based approaches (Bárdossy and Pegram, 2009), among others. Moreover, while these approaches improved the representation of spatial patterns, their application for high-temporal-resolution-dependent purposes is limited. The theory of point processes presents a framework to address this limitation, modeling both spatial and temporal representations using probabilistic distributions. For example, Cowpertwait et al. (2002) used a Poisson process to represent precipitation cells and the occurrence of rain. However, these models struggle to represent precipitation with complex patterns and consequently, precipitation fields are represented as random fields with parameterized covariance functions. For instance, (Koutsoyiannis et al., 2011) employed a Hurst-Kolmogorov process to represent rainfall fields, specifying values for the spatial covariance function. The literature also reports another class of methods employing the scale invariance theory, simulating rainfall through multifractal processes (Schertzer and Lovejoy, 1987). It should be stressed that while this approach yields satisfactory results, its application faces challenges, particularly in transitioning to practical use. Additionally, these methods require a significant amount of data and specific measurements, such as radar data. As reported by Ramanathan et al. (2022), many of the aforementioned methods are based on non-physical assumptions (*e.g.*, spatial independence of rainfall amounts in a single site and some multivariate WGs) which makes the lack of physical reality in the generation of precipitation a major hurdle in many hydrological applications. This has led to the introduction of new generators that respect the complexity of the physics involved in rainfall scenarios, see for example (Paschalis et al., 2013; Ramanathan et al., 2022). In the present work, we leverage on the ability of generative machine learning tools, especially Generative Adversarial Networks (GANs), to generate realistic climate scenarios (Besombes et al., 2021). These models have undergone significant improvement over time, tailoring them to specific data generation tasks across various domains (Aggarwal et al., 2021). In the context of generation of extreme samples, the main challenge limiting the adoption of GANs is the tendency of generated samples to follow a bounded or light-tailed distribution when the input noise, fed to the generator, follows a uniform or Gaussian distribution, respectively. Several studies have tried to solve this issue. For instance, Huster et al. (2021) proposed the use of heavy-tailed input to address this challenge whereas, Bhatia et al. (2021) and Boulaguiem et al. (2022) suggested a hybrid approach that combines advantages of the conditional GANs with the Extreme Value Theory (EVT) to overcome these limitations.

In the present study, we propose the implementation of the ExGAN model introduced by Bhatia et al. (2021), for the generation of synthetic Extreme Precipitation Events (EPEs) data. The attractiveness of this method can be summarized by two major advantages. Firstly, it has the capability to generate realistic extreme precipitation patterns even in areas with limited data overcoming many of the limitations identified in previous methods. Secondly, the proposed ExGAN is able to respect the probability as defined by the concept of a return period. This concept is often overlooked in physically-based methods for generating extreme precipitation patterns.The generated events will be then transformed into hydrological responses through the well-established SCS-CN model, see (Soulis and Valiantzas, 2012). In the current work, we employ this model due to its demonstrated capability to transform rainfall into runoff, particularly in situations involving flash floods and areas with limited data coverage, notably in the Mediterranean region. It should be noted that the effectiveness of this model in such contexts has been illustrated in previous studies (*e.g.*, (Singh et al., 2015; Shadeed, 2023)). Hence, implementing this model will enable us to expand the scope of findings of our study, even in regions with limited data availability. Risk mapping will be then carried out by forcing a hydrodynamic model that is well-calibrated in the region. In general, one-dimensional models are capable of accurately simulating river channels; however, river overflows can cause overland flows that spread extensively across floodplains. Moreover, as Oued Martil extends to the Mediterranean Sea, the downstream hydrodynamics exhibit a complex pattern and therefore, two-dimensional modeling is required which can be mathematically represented by the well-established shallow water equations in two space dimensions. In our case, these equations are numerically solved using the TELEMAC software which is an open-source hydrodynamics software based on the finite element analysis, see for example (Nguyen et al., 2018) and (Tung et al., 2015).

The suggested methods in the present work are applied over the very vulnerable area of Oued Martil valley. The Martil river (referred to as the Oued Martil) has a long history of flooding (Rian, 2021) and therefore, it is the primary focus of the current study. This river travels through the city of Tetouan and its surrounding provinces in northern Morocco before flushing into the Mediterranean Sea. The climate of this area is characterized by considerable variability at all time scales (El Moçayd et al., 2020). It has two distinct seasons: a rainy and humid season from October to April, and a generally dry season from May to September. The region is also highly vulnerable to extreme precipitation, which is known as the primary cause of flooding (Chaqdid et al., 2023). During these weather events, the upper atmosphere above the region is characterized by strong geopotential and wind speed anomalies associated with moisture flow and cyclonic activity, originating mainly from the North Atlantic. This situation occurs in particular during the negative phase of the North Atlantic Oscillation, see Region 1 in Chaqdid et al. (2023). The high variability of precipitation patterns in the region significantly impacts the local hydrology with the influence of the irregular topography characterizing the region and the impermeable nature of its soil as all contribute to the generation of significant runoff in the narrow Martil valley, as well as torrential and severe floods, see for instance (Karrouchi et al., 2016) and (Prokos et al., 2016). These events have caused enormous economical, ecological, and infrastructure devastations. Notice that although such events occur over a short period of time and their frequency is irregular, still their effects are tremendous, see for example (Rian, 2021).

The present paper provides background information on the study area, specifically addressing the flood event that occurred on March 1, 2021 in Oued Martil. Subsequently, it details the models employed for generating synthetic EPEs data, transforming them into discharge, and using the discharge for mapping flood risk in the Martil valley. To validate the models, a comprehensive comparison was conducted between the simulated outcomes and observed data as well as the results obtained through conventional meth-

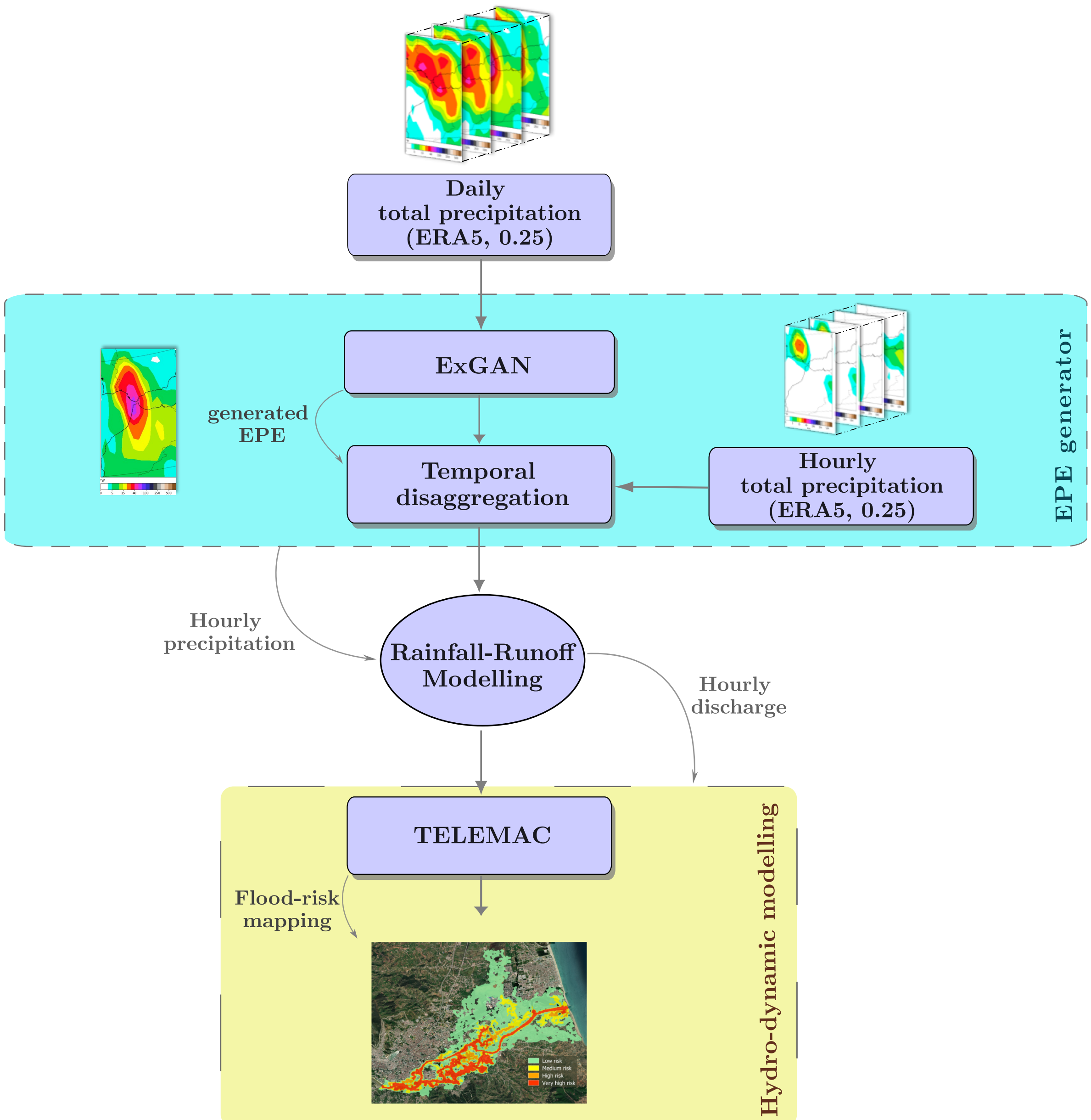

Figure 1: Flow chart of data and methodology used in the present study.

ods. This comparative analysis illustrates the reliability of our approach. A summary of the methods and data employed is depicted in Figure 1. The current work focuses on developing reliable flood risk mapping using the ExGAN approach. It discusses the generation of extreme precipitation through two methods of training the ExGAN: using either a gridded dataset or a single point dataset. A comparison between results obtained using our proposed model and those obtained using the standard WGs method is also conducted. The research outline is as follows: The second section presents the techniques and methods, including the study area, data sources, and modeling approaches. The third section covering the results and discussion is divided into three subsections. The first subsection presents various results regarding model calibration. The second subsection discusses the generation of synthetic precipitation data with ExGans. Finally, the third subsection presents the mapping of flood risk. The fourth section concludes the paper and outlines future perspectives.

2 Materials and methods

In this section we present the techniques and methodology used in the present study for developing a climate-informed flood risk mapping using a GAN-based approach. This includes the study area, data acquisition along with the methods used for the model.

2.1 Study area

The Oued Martil watershed is located in the northwest of the Riffian chain and it is surrounded by the Mediterranean Sea to the east, the high Rif to the south, the plains of Gharb to the west, and the mountains overlooking the Strait of Gibraltar to the north (Rian, 2021; Karrouchi et al., 2016). The watershed is characterized by a vast area spanning 1170 km^2 and rapidly varying topography ranging from 0 m in the coast to a maximum elevation of 1800 m in the south (Karrouchi et al., 2016). This area covers the cities of Tetouan and Martil, as well as 14 small communities counting for a total population of $445,000$ persons (Rian, 2021). At the upstream of the watershed, three principal tributaries (Khemis, Chekkour, and Mhajrate) contribute to the formation of the lower course of Oued Martil (Martil river). The river crosses the southern side of the city of Tetouan through the "Torreta" region (shown by zone B in Figure 2), before flowing into the Mediterranean Sea on the eastern side of the basin (shown by zone D in Figure 2) (Khattabi, 2021). The downstream of the river, in the southern part of Martil forms a delta, although nowadays the majority of its arms no longer communicate with the sea, see for example (Khattabi, 2021). The basic layout of this delta has experienced various hydrological changes throughout the years; a large part of the alluvial plain has been converted to agricultural land; an island of the delta has been developed into a residential area (Hay Diza); a channel at the south-eastern end of the delta, once isolated from the sea, is now almost dry except during rainy periods (Khattabi, 2021). Notice that the river channel includes many meanders. For instance, near its downstream (shown by zone D in Figure 2), there is an abandoned U-shaped meander (an oxbow lake) that is currently inactive except during seasons of heavy rainfall.

It should be stressed that the focal point of the present study is to simulate inundations of Oued Martil and therefore, the area considered was chosen such that the studied river channel drained from the Torreta bridge where a measuring station is located, and traveled downstream until it reaches the river outlet. The channel was approximately 10 kilometers long, and its width varied from 50 to 260 meters. For the floodplain, as depicted in Figure 2, we relied on two domains such that in the first stage of this study, the model was tested and validated on a narrow floodplain whose width ranges from 25 to 300 meters. Subsequently, to track flood progression and geographically locate areas with high risks of flooding, the floodplain was enlarged, in order to cover most of the cities of Tetouan and Martil. Here, on the left bank of the river, the width reaches 8.2 kilometers while on the right side, it reaches 4.6 kilometers. The narrow domain, delimited in blue in Figure 2, spanned an area of around 4.3 km^2 whereas, the large domain in yellow covered an area of 109.4 km^2.

2.2 Data processing

To generate synthetic EPEs, we utilize the ECMWF ERA5 reanalysis data (Hersbach et al., 2020) featuring a spatial resolution of $0.25^\circ \times 0.25^\circ$ and covering the period

Figure 2: Geographical location of the study area in Oued Martil valley (source: ESRI Satellite Imagery).

from 1979 to 2021. This choice is supported by the investigation conducted by (Tuel and El Moçayd, 2023), wherein they assessed nine gridded satellite-based and reanalysis precipitation datasets using 120 time series of precipitation data collected across the country. The findings in (Tuel and El Moçayd, 2023) suggest that ERA5 exhibits superior performance in capturing extreme precipitation dynamics compared to other analyzed datasets except for MSWEP, which shows comparable skill. Despite the higher spatial resolution of MSWEP ($0.11° \times 0.11°$), its unavailability at the hourly time step required for temporal disaggregation of generated events precluded its use. Consequently, to maintain methodological consistency in our study, we relied on ERA5 estimates both daily and hourly. Prior to conducting simulations on TELEMAC software, various input parameters must also be specified. This comprises data of the domain geometry which includes the bathymetry, configuration and computational mesh along with the hydraulics data that account for the initial and boundary conditions. The majority of these parameters have been made available thanks to extensive fieldwork conducted by the local watershed agency in Morocco known as the Agence du Bassin Hydraulique du Loukkos (ABHL). The latter has frequently proceeded with the evaluation of bathymetry at different points and the most updated data were used in this study.

As a starting point, the bathymetry of the computational domain was addressed through a special treatment of the provided raw data. Numerical data for 99 cross-sections of the river was extracted, covering the area between the Tamouda Bridge (zone A in Figure 2) and the river downstream at Martil (zone D in Figure 2). Each cross-section was defined based on cartesian coordinates, with several data points provided at each of these sections. However, these data are sparsely distributed across each cross-section and therefore, further data preparation and homogenization were performed following a two-stage methodology: The first stage involves refining the original ground data by removing erroneous information and unreliable cross-sections such as those representing the bridges. The second stage aims to homogenize the data collected along the river cross-sections. To achieve this step, spatial interpolation methods were used to select 17 points within each cross-section. Thus, each point identifies a characteristic property of the river shape such as the center of the riverbed, the delimiters of the riverbed, or the top of the banks, see Figure 3. For each cross-section, an interpolation method is chosen to adequately fit the properties of the considered section. We primarily used two types of interpolation: makima (Modified Akima piecewise cubic Hermite interpolation) and pchip (Piecewise Cubic Hermite interpolating polynomial). This approach ensures that the main structure of the river is accurately identified and robustly represented, while also separating the floodplain from the river channel. Considering that the hydraulic data were measured at the Torreta station, marked as zone

B in Figure 2, a new cross-section was subsequently created at the same location, as depicted in Figure 4, to represent the upstream boundary of the domain. Employing a methodology similar to the aforementioned one and using linear interpolation, we estimated the elevation values of the newly defined cross-sectional points. Accordingly, the computational domain, delineated in blue in Figure 2, was limited to the area between the Torreta station and the river mouth which served as the upstream and downstream boundaries for the hydraulic problem. To enhance flood risk assessment, a broader domain was established and this larger area includes additional data points, expanding the floodplain across the entire region delimited in yellow in Figure 2.

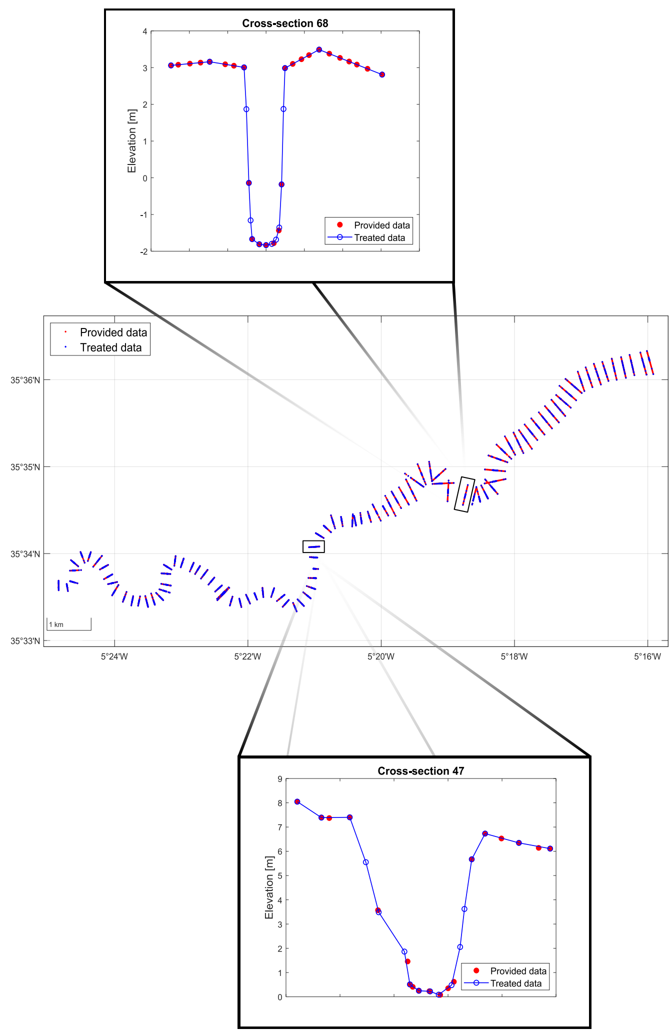

Figure 3: Comparison of bathymetric data from the Tamouda bridge to the river mouth, before and after the treatment.

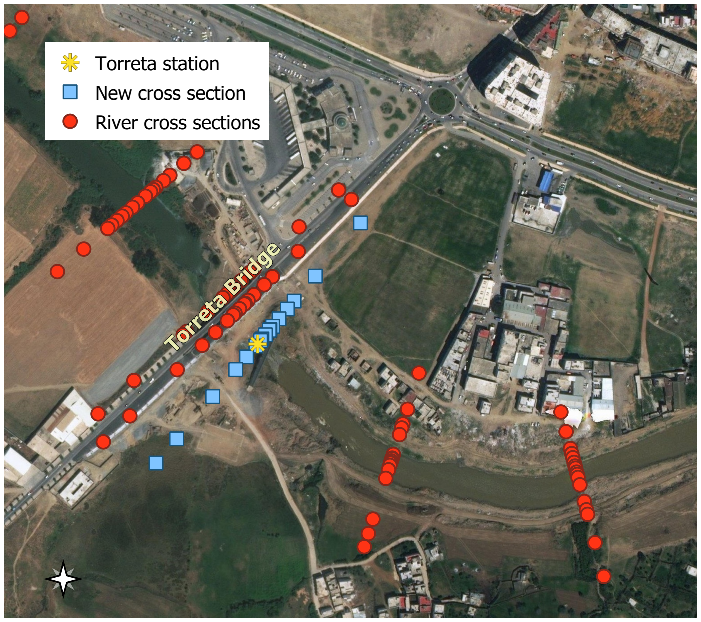

Figure 4: Construction of the new cross-section through the software QGIS.

To finalize the setup of the computational domains associated with the model, both domains were discretized to perform the necessary calculations. To achieve this, an unstructured mesh for the river channel was first created, which was used as a sub-mesh to generate a wider mesh enclosing the floodplain for both computational domains. This procedure was carried out using the software BlueKenue, developed by the Canadian Hydraulics Center (CHC) of the National Research Council to provide a framework for pre-processing, post-processing and data visualization of the hydrodynamics model (Barton, 2019). In Figure 5 and Figure 6 we display the resulting unstructured meshes used in our simulations. Here, the narrow domain contained 8977 nodes and 16751 triangular elements whereas, the second one enclosed 100857 nodes and 200346 elements.

Once the geometry of the domain is generated, hydraulics data are required to perform the numerical simulations. Our primary focus is on the flooding event that occurred on March 1, 2021. On that day, a rainy event occurred in Tetouan and its surrounding areas resulting in dramatic and severe flash floods. The city experienced an unusual

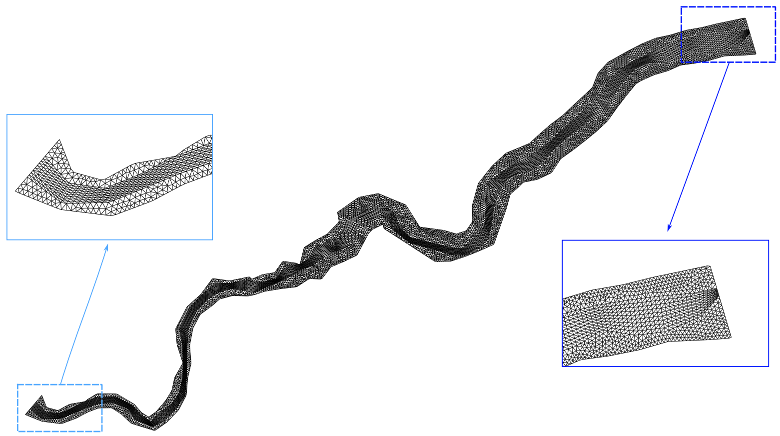

Figure 5: Computational mesh of the narrow domain (2D view).

rainy episode with 120 mm of local high-intensity rainfall recorded in 24 hours and a maximum of 79 mm recorded in two hours. The measurements of the flow rate were collected at Torreta station from 12:00 p.m. to 9:30 a.m. as shown in Figure 7. The river discharge attained a maximum peak of 516.41 m^3/s at 11:30 p.m. The provided time-dependent hydrograph was used as input to specify the river discharge at the upstream open boundary of the domain.

To determine the initial conditions, we conducted an independent simulation of the initial state of the river, a method commonly known as 'hotstart'. Note that this approach accelerates the calculations and it provides a stable baseline for unsteady simulations. The initial simulation involves a dry domain, allowing water to flow naturally from the inlet and follow the river channel. To prevent supercritical flow at the entrance, we have carefully defined the required upstream open boundary conditions for water depth and flow rate, setting minimum values for both of them. We then simulate a sufficiently long duration to reach an almost steady-state regime throughout the river which enhances numerical stability. Subsequently, to hotstart the main simulations, the result file of this initial simulation is used as the previous computation file in the main model.

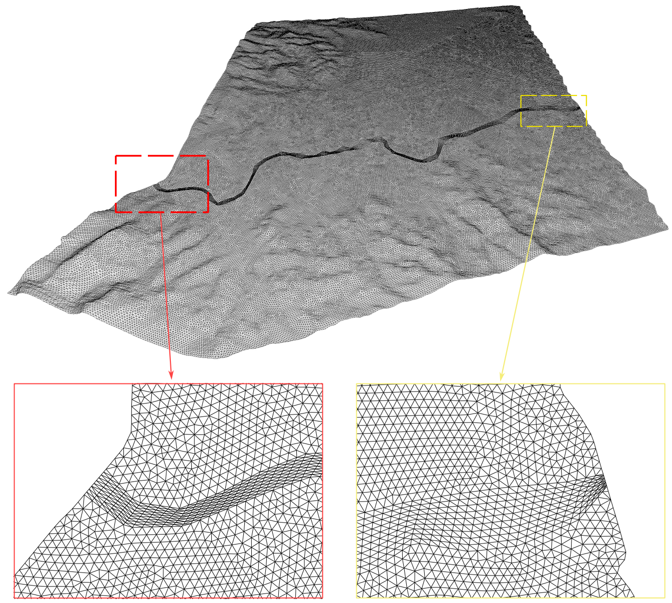

Figure 6: Computational mesh of the large domain (3D view).

2.3 Methods

We present the proposed methodologies for modeling of extreme precipitation events and rainfall-runoff along with the governing equations used for the hydraulics.

2.3.1 Modeling of extreme precipitation events

We propose a two-step approach for generating synthetic precipitation data. In the first step, we employ ExGAN, a conditional adversarial neural network developed by Bhatia et al. (2021) to generate daily extreme precipitation. The ExGAN utilizes a conditional Deep Convolutional Generative Adversarial Network (DCGAN) within an Extreme Value Theory (EVT) framework, focusing on learning from the tail of the distribution rather than its bulk and this distinctive feature is achieved through a distribution-shifting procedure. Using a shift parameter (c), this procedure iteratively 'shifts' the distribution by filtering out the less extreme $(1 - c)$ proportion of the data and generates additional data to restore the dataset to its original size. By repeating this process (k) times, the distribution is shifted by a factor of $(k \times c)$ toward the upper tail. (Bhatia et al., 2021) tested and validated their model on US precipitation data and

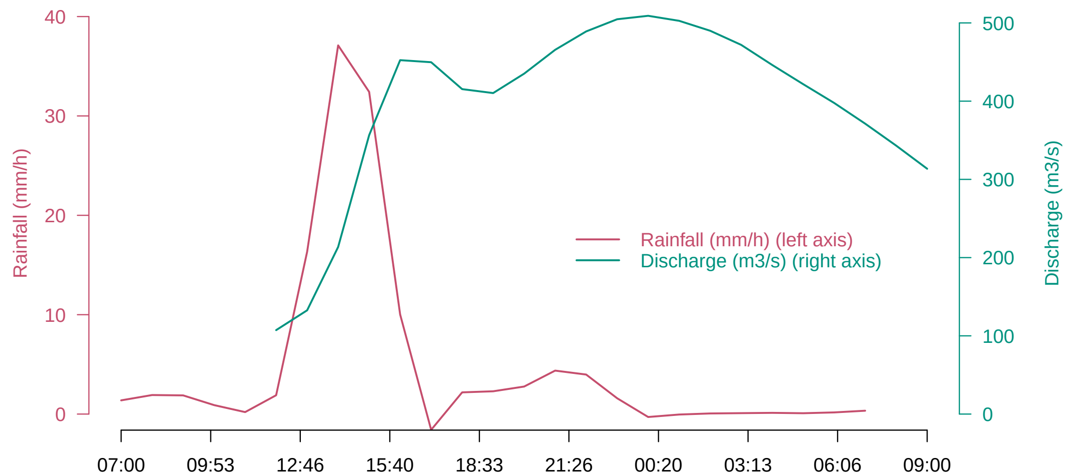

Figure 7: Rainfall and discharge at the Torreta station for March 01/02, 2021.

demonstrated its strong performance. Given the fact that we are also utilizing precipitation data, we adopted the same architecture proposed in their work to facilitate direct comparison of performance between our dataset and the one reported in (Bhatia et al., 2021). The generator is formed of four repeated sequences of a ConvTranspose layer with a 4×4 kernel size, followed by InstanceNorm and LeakyReLU activations. The final ConvTranspose layer outputs tensors normalized by a Tanh activation function. Conversely, the discriminator utilizes four repeated sequences of convolutional layers with a 4×4 kernel size alongside InstanceNorm and LeakyReLU activation. Additionally, it incorporates a single Conv4×4 layer followed by reshaping and concatenation processes, culminating in a linear layer that outputs probability scores through sigmoid activation. Further details on the architecture and implementation of ExGAN can be found in appendices included in Bhatia et al. (2021).

The discriminator and generator models are conditioned to incorporate extra inputs: a user-defined extremeness measure for the discriminator, and samples drawn from a Generalized Pareto Distribution (GPD) fitted to the extremeness measure computed over the shifted data for the generator. In the present study, we consider two measures of extremeness. The first measure, as proposed in (Bhatia et al., 2021), computes the total rainfall in the region (16W, 0E, 24N, 40N), referred to herein as the Regional

Extremeness Measure. The second measure considers precipitation only in the pixel where the Torreta station is located (5.372W, 35.558N), referred to herein as the Local Extremeness Measure. Furthermore, while Bhatia et al. (2021) resized their input data, we opted against this approach to avoid potential loss of information about local extremes that may result from the averaging procedure.

Unfortunately, ExGAN does not allow for the generation of a sequence of events and instead, it can only produce individual hourly or daily EPEs as independent random variables. However, TELEMAC requires discharge data with at least an hourly time step for a 24-hour EPE to accurately assess the flood risk. To circumvent this limitation, we implement a temporal disaggregation procedure as the second step of our approach. This disaggregation process uses ERA5 hourly total precipitation data, following the steps outlined in Algorithm 1. In the first step, the algorithm identifies a real EPE from ERA5 that is most similar to the generated event, first in terms of spatial pattern, and then in terms of precipitation value. More precisely, we define extreme precipitation events as days with precipitation greater than or equal to the 99th percentile of wet days ($> 1\ mm$) and from these events, we identify the five EPEs that spatially overlap the most with the generated event. Then, we choose the one that minimizes the mean square error between the generated event and real event precipitation. In the second step, we use the chosen event and its corresponding hourly precipitation distribution from ERA5 to disaggregate the generated event, using the following equation:

$$Pg_{i,t} = \frac{\mathrm{Pr}_{i,t}}{\mathrm{Pr}_{i,24h}} Pg_{i,24h}, \qquad 1 \leq t \leq 24, \tag{1}$$

where $Pg_{i,t}$ is the precipitation at gridpoint i and at t hour of the generated event, $Pg_{i,24}$ is the 24-hour total precipitation of the generated event at gridpoint i, $Pr_{i,t}$ is the precipitation at gridpoint i and at t hour of the real event, and $Pr_{i,24}$ is the 24-hour total precipitation of the real event at gridpoint i. Overall, the convolutional architecture of ExGAN enables it to learn complex dependence structures within images. In contrast to the conventional WGs, the ExGAN facilitates the modeling of patterns and spatial dependence in rainfall events across a wide geographical area. This capability allows the generation of local EPEs that maintain consistency with large-scale patterns of the precipitation. Additionally, the use of the normalized 24-hour distribution of precipitation from ERA5 ($\frac{\mathrm{Pr}_{i,t}}{\mathrm{Pr}_{i,24h}}$ in equation (1)) enables us to preserve sub-daily rainfall variability.

To evaluate ExGAN and validate its performance, we employ the Frechet Inception Distance (FID) to quantify the ability of the generator to replicate the tail of the precipitation distribution. We utilize the Reconstruction Loss to assess its capability in reconstructing unseen extreme samples. Additionally, we conduct visual inspections by comparing animations of generated events with real events. It should be stressed that the FID does not directly compare real and generated images; instead, it compares the distributions of their features which are assumed to be approximated by Gaussian distributions. Both real and generated images undergo feature extraction by a pre-trained model and their feature distributions are then compared by computing a distance metric based on their means and variances. Due to the specific nature of the precipitation dataset, Bhatia et al. (2021) proposes an alternative to the conventional use of an ImageNet-pretrained Inception network for FID calculation. Bhatia et al. (2021) suggested employing an autoencoder constructed and trained on the test data which they argue is more suitable for effectively evaluating the generator, particularly in the context of precipitation data. Inception-v3 (Szegedy et al., 2016), trained on ImageNet dataset, is commonly used to compute FID, enabling comparison between generative models with the one achieving a lower FID considered to perform better. Typically, the obtained FID values are compared with a baseline or a previous state-of-the-art model. However, since Bhatia et al. (2021) did not use an ImageNet-pretrained Inception network, they compared the FID of the ExGAN with a baseline model (DC-

GAN) and found that ExGAN performs better. In the current study, we use the same autoencoder model as Bhatia et al. (2021) to calculate the FID, enabling a comparison of the performance of ExGAN on our dataset with that of Bhatia et al. (2021). The FID is computed using the statistics derived from the bottleneck activations of the autoencoder as expressed by the following formula:

$$\mathrm{FID} = \|\mu_r - \mu_g\|^2 + \mathrm{Tr}\Big(\Sigma_r + \Sigma_g - 2\,(\Sigma_r\Sigma_g)^{1/2}\Big).$$

Here, Tr represents the trace of a matrix, (μ_r, Σ_r) and (μ_g,Σ_g) are the mean and covariance of the bottleneck activations for real and generated samples, respectively. For an extremeness-conditioned generator G, the reconstruction loss is given by

$$\mathcal{L}_{\text{rec\_ext}} = \frac{1}{m}\sum_{i=1}^{m}\min_{z_i}\Big\|G(z_i, E(\tilde{x}_i)) - \tilde{x}_i\Big\|_2^2,$$

where $(\tilde{x}_1, \ldots, \tilde{x}_m)$ represent the test images, z_i denotes the latent space vectors, and E is the extremeness measure.

2.3.2 Rainfall-runoff modeling

The SCS-NC model (SCS, 1972) is one of the simplest and most widely used models for rainfall-runoff modeling. This model was first introduced by the Natural Resources Conservation Service, or NRCS (previously known as the Soil Conservation Service, SCS) and is formulated by

$$Q = \begin{cases} \dfrac{(P - 0.2S)^2}{P + 0.8S}, & \text{if} \quad P > 0.2S \\[2ex] 0, & \text{if} \quad P \leq 0.2S, \end{cases} \tag{2}$$

where Q is the direct runoff or rainfall excess, P is the total precipitation during a rainfall event, and S is the potential maximum retention after runoff begins, which is related to the land use, soil, and antecedent moisture conditions. It is often expressed as the curve number (CN). This model was revisited by Hawkins et al. (2002) and the revision indicates that the model is less sensitive to lower precipitation and lower curve numbers (CNs). Thus, Hawkins et al. (2002) proposed reducing the initial abstraction (I/S) from 20% to 5% and the changes to the SCS-CN model that follow this choice are as follows:

$$Q = \begin{cases} \dfrac{(P - 0.05S_{0.05})^2}{P + 0.95S_{0.05}} & \text{if} \quad P > 0.05S \\ \\ 0, & \text{if} \quad P \leq 0.05S, \end{cases} \tag{3}$$

where the relationship between $S_{0.05}$ and $S_{0.02}$ is given by

$$S_{0.05} = 1.33{S_{0.20}}^{1.15}.$$

It should be noted that since our study relies on gridded data, it is important to note that the precipitation values are not specific to a single location but rather represent grid-averaged values. Consequently, the precipitation values during EPEs are lower than the locally observed values. As a result, the modified approach proposed by Hawkins et al. (2002) is particularly well-suited for our study.

2.3.3 Hydraulic modeling

In the present study, the TELEMAC-2D is considered one of the most useful tools for modeling complex hydrodynamics. It effectively simulates free-surface flows in two dimensions of horizontal space in different water bodies including rivers, estuaries, and coastal areas (Tung et al., 2015). At each node of the computational mesh, the computational model estimates the water height and the two velocity components, following the resolution of the two-dimensional shallow water equations (Nguyen et al., 2018). Note that TELEMAC-2D has been widely used in modeling hydraulis including a variety of applications including flooding. In general, the governing equations of shallow water flows are derived by balancing the net inflow of mass and momentum through the boundaries of a control volume whilst accounting for shallow water assumptions. This class of equations uses the assumption that the vertical scale is much smaller than any typical horizontal scale and can be derived from the depth-averaged incompressible Navier–Stokes equations subject to a hydrostatic pressure. Thus, the shallow water equations considered in this study read

$$\begin{aligned} \frac{\partial h}{\partial t} + U \cdot \nabla(h) + h\,\mathrm{div}(u) &= S_h, \\ \frac{\partial u}{\partial t} + U \cdot \nabla(u) - \frac{1}{h}\,\mathrm{div}\left(h\nu_t \nabla u\right) &= -g\frac{\partial Z}{\partial x} + S_x, \\ \frac{\partial v}{\partial t} + U \cdot \nabla(v) - \frac{1}{h}\,\mathrm{div}\left(h\nu_t \nabla v\right) &= -g\frac{\partial Z}{\partial y} + S_y, \end{aligned} \tag{4}$$

where h (m) is the water depth, u and v (m/s) are depth-averaged velocities in the x- and y-direction, respectively. In (4), g (m/s^2) is the gravity acceleration, ν_t (m^2/s) is the diffusion coefficient, Z (m) is the free-surface elevation ($Z = h+z$, with z represents the bathymetry), t (s) is time, x are y (m) are space coordinates, S_h (m/s) are source or sink of fluid, h, u, v are the unknowns. Here, S_x and S_y (m/s^2) are source terms representing the wind, Coriolis force and bottom friction among others. For a detailed description of these equations and the implementation of the numerical solver used in our TELEMAC simulations, we refer to Hervouet (2007).

3 Results and discussion

This section delineates and examines the outcomes of our study in line with the previously outlined methodology. Initially, sequential calibration of the rainfall-runoff model and the hydraulic model are conducted. This calibration involves fitting both models to diverse observations of precipitation, runoff, and water levels obtained from a historical flooding incident (March 1, 2021). Subsequently, the generation of EPEs is deliberated upon and various events are generated under distinct scenarios aligning with different

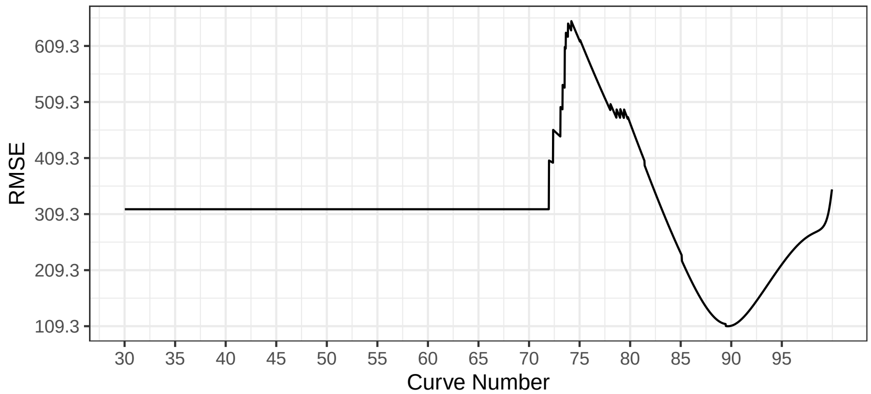

Figure 8: Variation of RMSE with curve number. Here, the RMSE is computed between hourly discharge and runoff which is estimated using ERA5 precipitation and the SCS-NC model for March 1, 2021 flood event.

thresholds corresponding to varied return periods. Finally, these scenarios will serve as inputs for the models facilitating the evaluation of risk mapping within a vulnerable region.

3.1 Simulation of a past flood event

To simulate runoff using the SCS-NC model, it is essential to compute the curve number for the watershed, considering factors like land use, soil type, and hydrological conditions. However, relying on grid-averaged data often yields lower precipitation values compared to local observations. Consequently, it becomes imperative to calibrate the curve number based on ERA5 precipitation for our watershed. Note that without proper calibration, there is a risk of complete precipitation absorption, leading to minimal or no runoff. The calibration process involves minimizing the Root Mean Square Error (RMSE) between observed hourly discharge values and runoff estimated from ERA5 precipitation data during the EPE that occurred in Torreta on March 1, 2021. The optimized curve number value obtained through this calibration process is 90 (refer to Figure 8). This specific curve number will subsequently be applied in the SCS-CN model to convert the generated EPEs into runoff.

Next, the calibration and validation of the TELEMAC-2D hydraulic model are conducted and due to limited access to data, both processes are performed simultaneously using the March 1, 2021, event as a reference. Since data were collected at the Torreta station, we verified the accuracy of the computed flow rates and water depths upstream of the river. For this purpose, we suggested extracting from the stage-discharge curve the estimated water depth values corresponding to the provided hydrograph and comparing them against the computed values. Moreover, for the flow rate, we compared the discharge values described in the hydrograph with the ones calculated by the model. For an adequate comparison of the computed and measured values, we calculated the root mean square error and we determined the optimal parameters for simulations of Oued Martil based on the trial-and-error method. In making our choices, we considered the RMSEs for the water depth and the discharge as well as the simulation time cost. For instance, we have successfully reduced the time lapse from more than 10 hours to approximately 1 hour. The majority of the parameters were identified using the first narrow study zone, where simulation execution time is substantially shorter (2 minutes compared to 1 hour for the other vast domain). The coefficient of friction was the only parameter that differed between the two domains. The other parameters had nearly the same impact on the findings of the model in both areas.

To model the friction on the bed, the Manning equation is used and the friction coefficient is assumed to be constant in time and space. The value of the coefficient was determined based on several simulations with different values of the Manning coefficient. We varied the friction coefficient in both domains and Table 1 summarizes the root mean square errors of the computed water depths and discharges for the tested simulations. For the narrow domain, we ranged the friction coefficients between 0.01 and 0.013, while for the large study area, we varied the coefficients between 0.038 and 0.041. Figure 9a and Figure 9b illustrate how the results obtained shifted in each case. The values that generate results in close agreement with the observations are 0.012 for the narrow

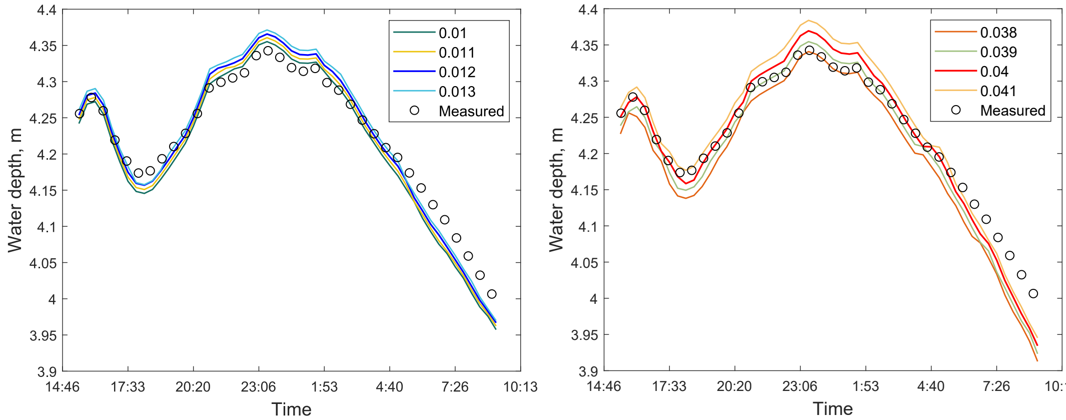

(a) Narrow domain

(b) Large domain

Figure 9: Different simulations of the water level during the flooding events using different values for the Manning coeffficient in the Narrow domain (a) and in the larger Domain (b).

Table 1: Comparison of friction coefficients based on RMSEs in the water depth in meters and in the discharge in cubic meters per second.

Narrow domain

Manning coefficient	RMSE in the discharge	RMSE in the water depth
0.01	1.6312	0.0230
0.011	1.6313	0.0210
0.012	1.6316	0.0199
0.013	1.6316	0.0211

Large domain

Manning coefficient	RMSE in the discharge	RMSE in the water depth
0.038	1.6311	0.0327
0.039	1.6343	0.0254
0.04	1.6333	0.0220
0.041	1.6325	0.0263

domain and 0.04 for the large domain. The adopted model following the calibration and validation procedures produces minimal errors in both domains in computing the water depths upstream of Oued Martil. The error was around 2 *cm* in the first computational domain and about 5 *cm* in the second. As depicted in Figure 9a and Figure 9b, the

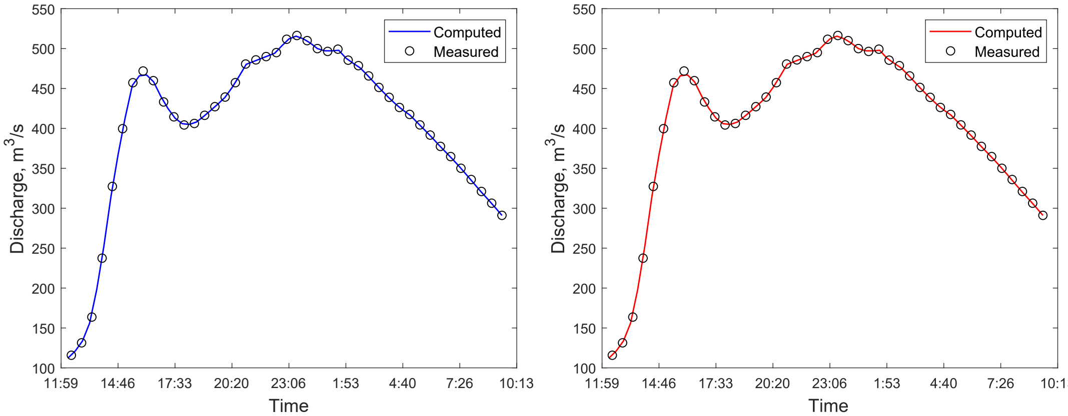

(a) Narrow domain

(b) Large domain

Figure 10: Comparison of the modeled and measured flow rates.

computed water depths with the TELEMAC-2D model are remarkably close to the estimated measured values. As for the flow rate, Figure 10a and Figure 10b show the near-perfect agreement between the computed and measured inflows which indicate that the flow has been properly adapted.

In the narrow study area, the calculated error was around 1.64 m^3/s. The first peak inflow was 465.93 m^3/s whereas, the first peak outflow was only 125.50 m^3/s. It required approximately 6250 seconds (1 hour, 44 minutes and 10 seconds) to traverse the modeled section of the river from Torreta to the sea. In the second area, the error was likewise close to 1.64 m^3/s but less outflow occurred than in the narrow one. Here, the estimated maximum value was 71.41 m^3/s whereas, the maximum in the other domain was 147.42 m^3/s. It further shows that the first domain constrained the movement of the water, whereas the second one allowed significant water dispersion across the entire domain. This allows a sufficient degree of reliability on the ability of the hydrodynamics model to simulate flood events.

3.2 Generation of synthetic precipitation data with ExGAN

The ExGAN was trained on 80% of daily precipitation data from ERA5 spanning the years 1979 to 2021, exclusively using days for which precipitation exceeded 1 mm at the Torretta station pixel (comprising 2730 days). For validation, a 20% subset of the dataset, covering the years 2013 to 2021, was set aside. The complete test dataset was employed for training the autoencoder for Fréchet Inception Distance (FID) calculation, while only days exceeding the 95th percentile of precipitation at the Torretta station pixel (totaling 149 events) were utilized to test the EPEs generated by ExGAN. The EPEs were identified by exceeding a predefined threshold on wet days (precipitation $> \ mm$). To condition both the generator and discriminator, two distinct extremeness measures were employed namely, a local measure, conditioning ExGAN directly on precipitation at the Torretta station pixel, and a regional extremeness measure, conditioning ExGAN on total precipitation across the entire region. Default settings recommended by Bhatia et al. (2021) were employed for noise distribution, activation functions, learning rates, noisy labels, and gradient clipping, we refer to Bhatia et al. (2021) for further details. However, fine-tuning of the distribution-shifting parameters (c and k) was conducted. Multiple iterations of ExGAN were trained with varying c and k values for both extremeness measures and the model performance was evaluated using the reconstruction loss function and FID as defined in section 2.3.1. It should also be stressed that the lower values of these metrics indicate superior performance.

Overall, the values of FID and Reconstruction Loss for ExGAN trained on our dataset, utilizing both extremeness measures, are lower than those reported by Bhatia et al. (2021), see Figure 2. This suggests superior performance of ExGAN on our dataset and this improvement can be attributed to several factors: firstly, we have not resized our input data and secondly, the model was exclusively trained on wet days in the Torreta station. These factors collectively reduced the spatial and temporal variability present in the dataset, thereby enabling ExGAN to achieve better performance. Regarding the selection of the optimal combination of c and k for our dataset: for the regional measure, we selected the pair ($c = 0.75$, $k = 10$), as this combination minimizes both the FID and Reconstruction Loss function without significantly altering a large proportion of the

Table 2: Comparison between results obtained using the proposed model and the model reported in Bhatia et al. (2021) for the reconstruction loss and FID values obtained by training ExGAN on Morocco precipitation for different values of c and k, and two extremeness measures.

	Extremeness measure	c	k	Rec.Loss	FID	Training dataset size (>1mm)	test dataset size (>P95)
Our dataset	Regional Extremeness Measure	0.24	2	0.0053	0.0354 ± 0.0002	2730 events	149 events
		0.49	4	0.0078	0.0243 ± 0.0003		
		0.75	10	0.0075	0.0221 ± 0.0003		
		0.9	27	0.0108	0.0182 ± 0.0002		
Bhatia et al. (2021)		0.24	2	0.0173	0.0367 ± 0.0096	2557 events	
		0.49	4	0.0173	0.0304 ± 0.0109		
		0.75	10	0.0172	0.0236 ± 0.0037		
		0.9	27	0.0169	0.0223 ± 0.0121		
Our dataset	Local Extremeness Measure	0.1	2	0.0021	0.0356 ± 0.0002	2730 events	149 events
		0.24	2	0.002	0.0240 ± 0.0003		
		0.49	4	0.0028	0.0368 ± 0.0001		
		0.75	10	0.0027	0.0306 ± 0.0003		
		0.9	27	0.0024	0.0262 ± 0.0004		

original dataset. On the other hand, for the local measure, we chose the pair ($c = 0.25$, $k = 2$).

The entire generation process, for different thresholds, encompassing the generation of daily totals and hourly disaggregation, underwent visual inspection through the animated evolution of hourly totals for events generated at different return periods. An illustration of the generated events can be found in Figure 12. Spatially, the results demonstrate a high degree of coherence and similarity to real events, suggesting that the models effectively learned the spatial patterns of EPEs in the region, compare Figure 12. Indeed, the model was able to reproduce similar patterns of precipitation to those observed in northern Morocco. Notice that such patterns are known to be generated by a westerly flow of moist air masses transported from the North Atlantic which then encounter the Rif mountains in northern Morocco and the Betic and Sierra Morena mountain chains in southern Spain resulting in this distinctive pattern of precipitation. Temporally, the implemented disaggregation procedure enabled us to preserve the mean 24-hour distribution of rainfall in Oued Martil valley (see Figure 11) while

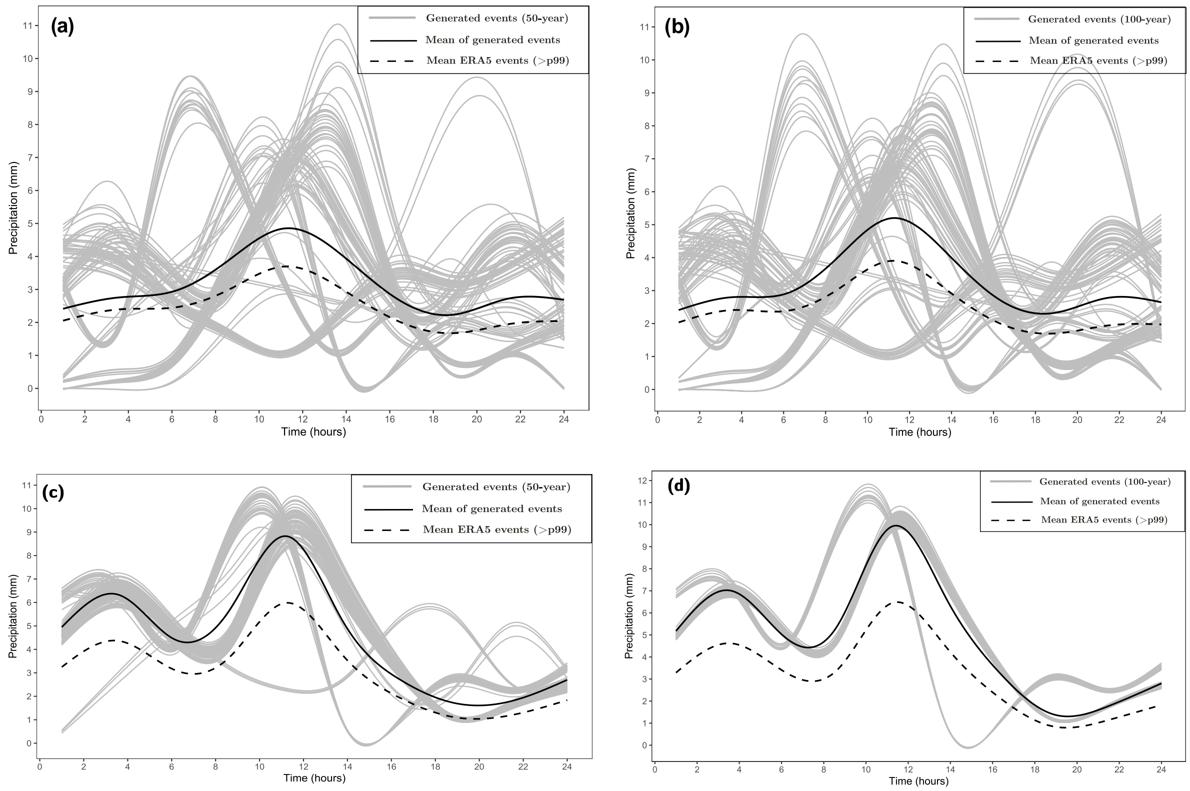

Figure 11: Hyetographs of 100 generated EPEs at Oued Martil valley using ExGAN conditioned in (a)-(b) the Regional Extremeness Measure, in (c)-(d) the Local Extremeness Measure. Here, (a) and (c) 50-year EPEs, and (b) and (d) 100-year EPEs. The generated EPEs are depicted in grey colors, their mean is represented by a solid black line, and the mean of ERA5 EPEs (> 99th percentile) used for disaggregation is shown by a dashed black line.

generating a sufficient number of random events consistent with the large-scale patterns of precipitation in the region.

Using the calibrated SCS-CN model, the generated EPEs were transformed into runoff signals as illustrated in Figure 13. This figure also depicts the runoff generated by the event with maximum daily precipitation in Torreta. It is also evident that the runoff produced by the EPEs generated using the Local Extremeness Measure exceeds the maximum observed runoff whereas, all runoffs produced using the Regional Extremeness Measure respect the climatology of precipitation in Torreta. Note that this runoff data will serve as upstream discharge forcing for the hydrodynamics model used in the flood risk mapping.

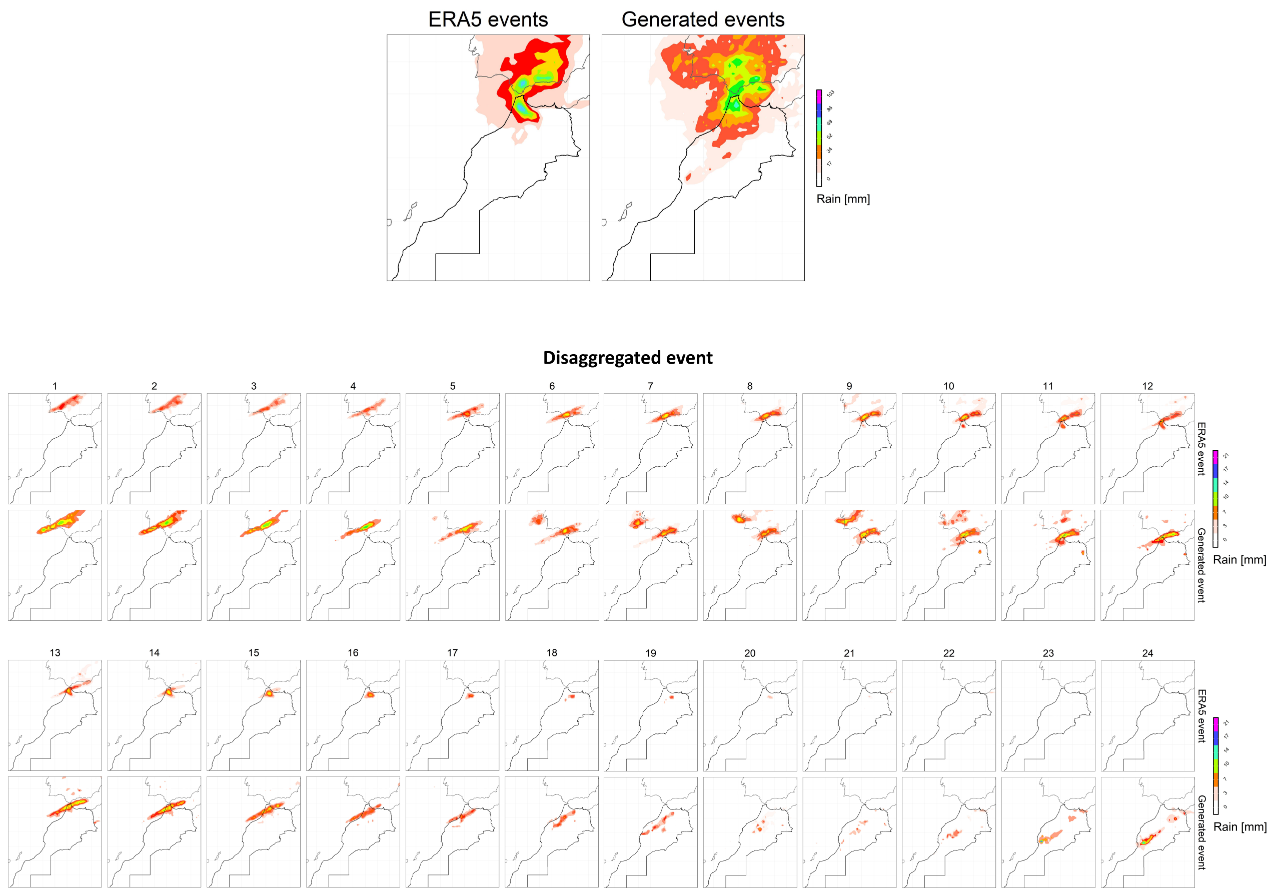

Figure 12: Example of the generation of an EPE using the Regional Extremeness Measure. At the top, is the daily total precipitation of the generated event (10-year return period) and the real event used to disaggregate it followed by the result of the disaggregation (see Algorithm 1).

3.3 Results and discussion for flood risk mapping

Implementing synthetically generated EPEs via ExGAN and their conversion into discharge time series, the calibrated model was tasked with forecasting ensuing hydrodynamics. This comprehensive methodology encompassed the assessment of diverse scenarios reflecting extreme precipitation incidents, each linked to probability values established by well-defined return periods. This approach facilitated an insightful examination and mapping of potential flood risks. In this section, the focus is on the resultant risk mapping. As a starting point, a return period of 50 years is examined. Employing the hydrodynamics model (TELEMAC), water depth calculations were per-

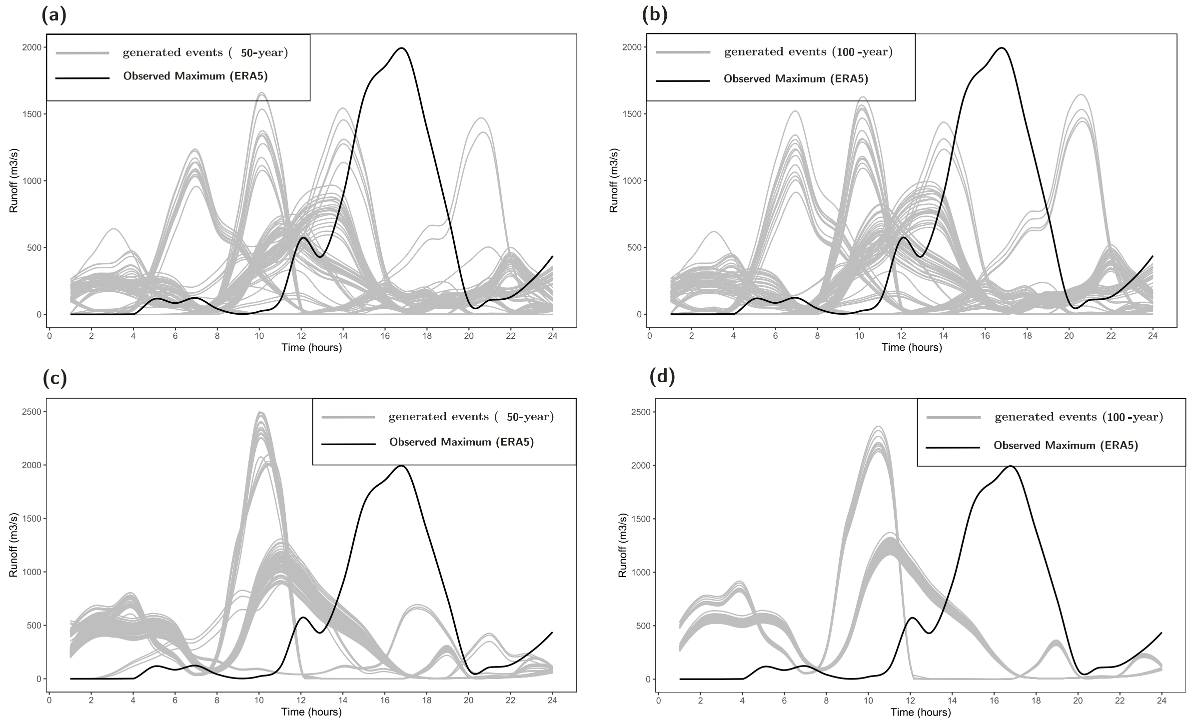

Figure 13: Runoff generated at Oued Martil valley by the EPEs depicted by grey lines in Figure 11. These EPEs are generated using ExGAN conditioned on (a-b) the Regional Extremeness Measure and (c-d) the Local Extremeness Measure. Panels (a-c) show 50-year EPEs, and panels (b-d) show 100-year EPEs. The runoff resulting from the event with maximum daily precipitation in Toretta is represented by a black line.

formed for each of the 100 scenarios outlined by the ExGAN. These depth values were subsequently transformed into discharge time series, serving as inputs for the model. Moreover, the expected values of the anticipated water depth and standard deviation were estimated based on the corresponding 100 simulations. In addition, the results are presented for both generation methods: the Local Extremeness Measure and the Regional Extremeness Measure. The outcomes of these simulations are presented in Figure 14 and as anticipated, areas near the river exhibit higher values for expected water levels, potentially surpassing 1.5 m in some instances, compare Figure 14a. Notably, a distinct depression is observable south of the Martil river, underscoring the necessity for preventative measures in this region to alleviate potential flood-related repercussions. The robustness of these results is bolstered by the standard deviation values (compare Figure 14b), all below 25 cm. Furthermore, the results exhibit an excessive risk when the Local Extremeness is used for the generation of extreme precipitation. This is observed in Figure 14c, where the wet region is notably greater than those presented in Figure 14a. However, as it is seen in Figure 14d, the standard deviation is not much affected by the kind of generation.

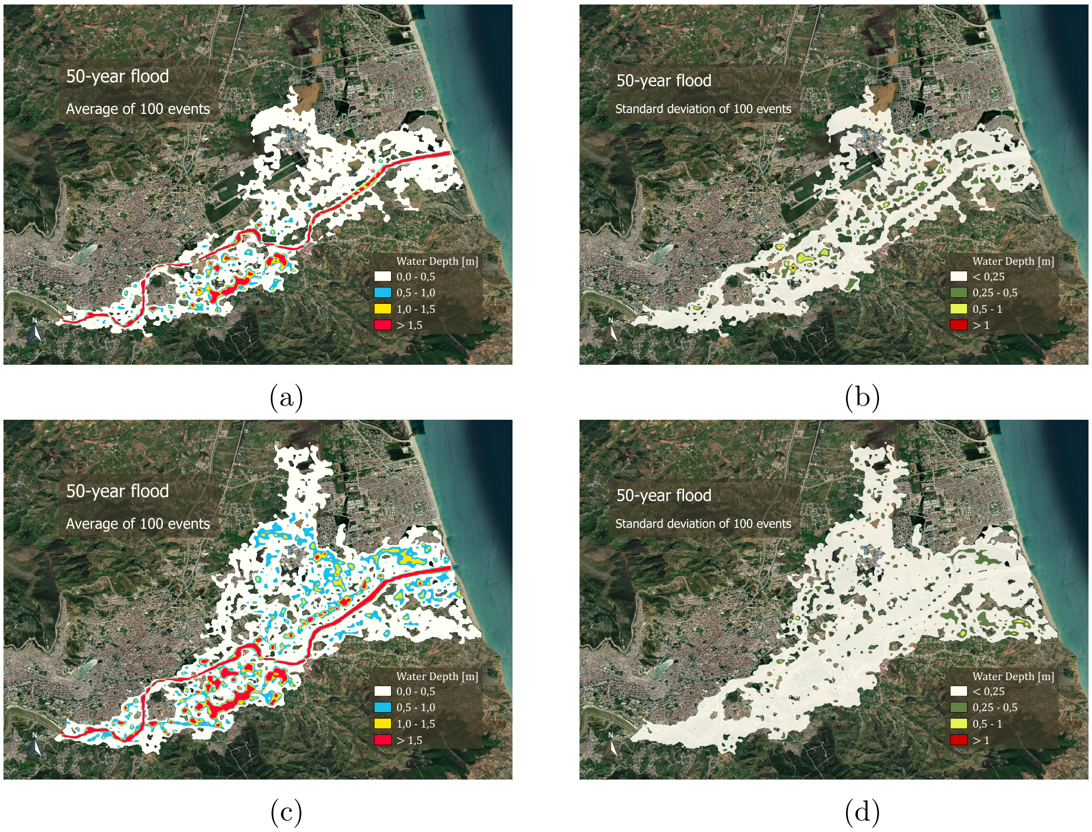

Figure 14: Expected water depth (a) and (c) along with the standard deviation (b) and (d) calculated for the multiple simulations of the hydrodynamics in the considered region corresponding to a return period of 50 years. Here, EPEs are generated using ExGAN conditioned on (a)-(b) the Regional Extremeness Measure, and (c)-(d) the Local Extremeness Measure. The extension of the flood is plotted over the natural domain of the region using a map derived from ESRI Satellite Imagery.

To facilitate risk mapping, the region has been categorized into four distinct segments, predicated upon the temporal average of the expected water depth values serving as a valuable indicator of potential flood occurrences. This methodological approach, widely prevalent in the literature, demonstrates its efficacy and adaptability in the realm of water management. The flexibility of this approach allows for the incorporation of

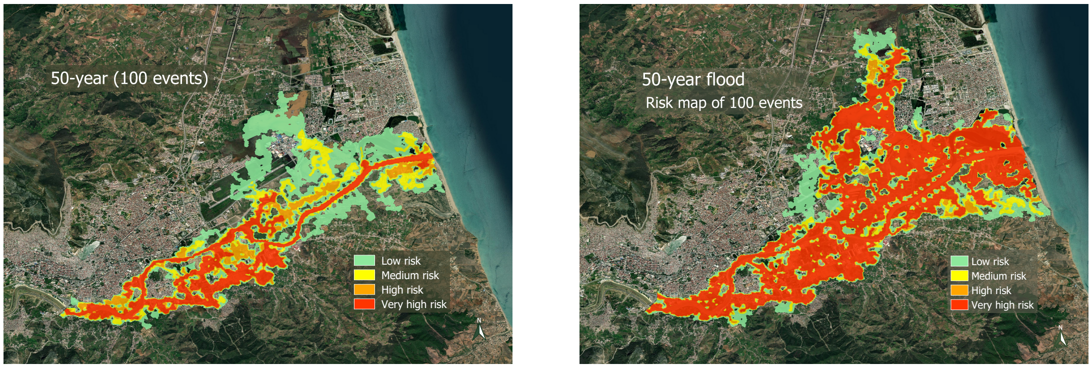

(a) (b)

Figure 15: Flood risk map corresponding to 50 years return periods generated for Oued Martil valley. EPEs are generated using ExGAN conditioned on (a) the Regional Extremeness Measure, and (b) the Local Extremeness Measure. The extension of the flood is plotted over the natural domain of the region using a map derived from ESRI Satellite Imagery.

diverse metrics to derive comprehensive flood risk maps, as documented in studies such as (Aronica et al., 2012). In the context of this study, the same approach is applied here in order to facilitate assessing the level of risk. The results are presented in Figure 15 using the two methods for the generation of extreme precipitation. The presence of a localized depression in the southern region of the Martil river unequivocally indicates a region of significantly high risk. In addition, certain areas in the northern part exhibit a comparatively minor susceptibility to flooding. These classifications elucidate the varying degrees of risk across the studied region, providing a nuanced understanding of potential flood hazards. The overestimation of the risk discussed before is translate in the maps, as the one produced using Local Extremeness Measure exhibit a high level of risk.

Given the susceptibility of the region to flooding, as highlighted in previous studies (refer to (Satour et al., 2021, 2023)), our investigation extends to flood mapping using a 100-year return period threshold and the outcomes are visualized in Figure 16 and Figure 17. These findings reveal an expansion of risk exposure towards the northern and eastern sectors of the studied region. Notably, there is no discernible escalation

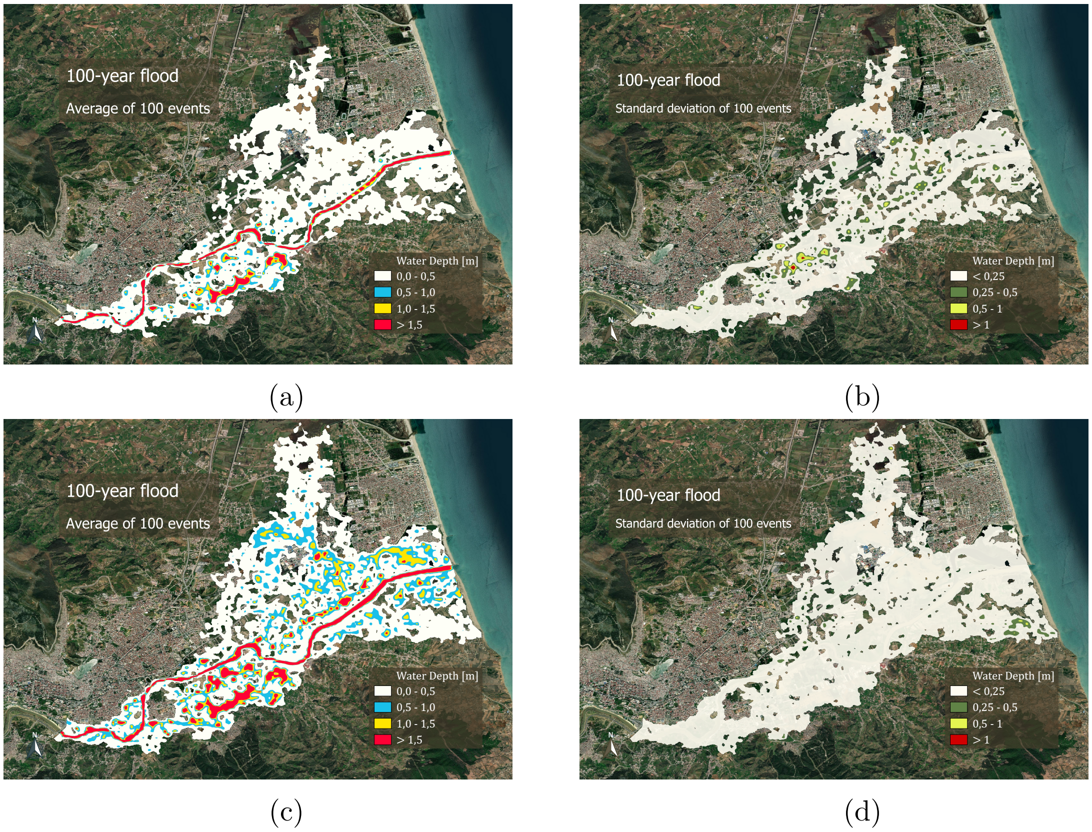

Figure 16: Same as Figure 14 but for a return period of 100 years.

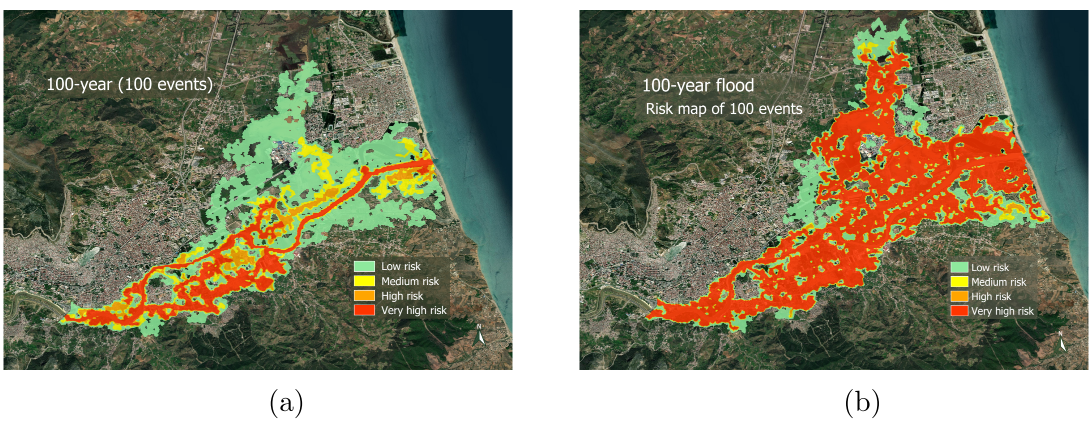

Figure 17: Same as Figure 15 but for a 100 years return period.

in risk levels within the areas previously covered by the assessment of 50-year return period. The robustness of these outcomes is underscored by consistently low standard deviation values, reflecting a high level of confidence in the results obtained. It is important to emphasize that the uncertainty presented in this analysis aligns with the local climatological patterns of extreme precipitation within the region. As for the comparison between the result using the generation with Local Extremeness Measure and Regional Extremeness Measure, the same overestimation expressed by the hydrographs is translated on the risk. Figure 17b displays a level of risk wider and higher than the one translated in Figure 15a. It should be noted that while this study primarily focuses on flood mapping through EPEs, other hydrodynamic parameters could potentially be addressed. However, such considerations lie beyond the scope of this specific study but interested readers seeking a comprehensive discourse on various expected uncertainties in flood modeling are referred to (Apel et al., 2004). Furthermore, it is crucial to note that epistemic uncertainty, as highlighted in the aforementioned reference, stands as a significant factor that can significantly influence overall results. This particular uncertainty encompasses the sampling strategy for river discharge, which directly originates from the variability in precipitation patterns. Indeed, both hydrological and hydrodynamic models are prone to uncertainty arising from various factors. Numerous studies have emphasized the importance of quantifying uncertainty in this context, as it allows for the assignment of a confidence level to each model simulation. Previous research has shown that uncertainties in discharge and friction coefficients can significantly affect the estimation of water levels, which are crucial for determining flood risk (as demonstrated by Roy et al. (2018)). Similar findings have been observed regarding bathymetry uncertainties, as discussed in Al-Ghosoun et al. (2021)). However, when extreme precipitation scenarios are present, the uncertainty associated with the corresponding hydrodynamic simulations remains unclear, necessitating a thorough understanding of its impact on flood risk mapping.

Finally, a comparative analysis between the risk mapping derived from ExGAN and the conventional sampling methodology referred hereafter by Monte-Carlo simulations is undertaken. To accomplish this, 100 hyetograph realizations are generated using a specific protocol such as initially, a daily precipitation event with a 100-year return period is selected. Subsequently, temporal disaggregation is executed by applying a

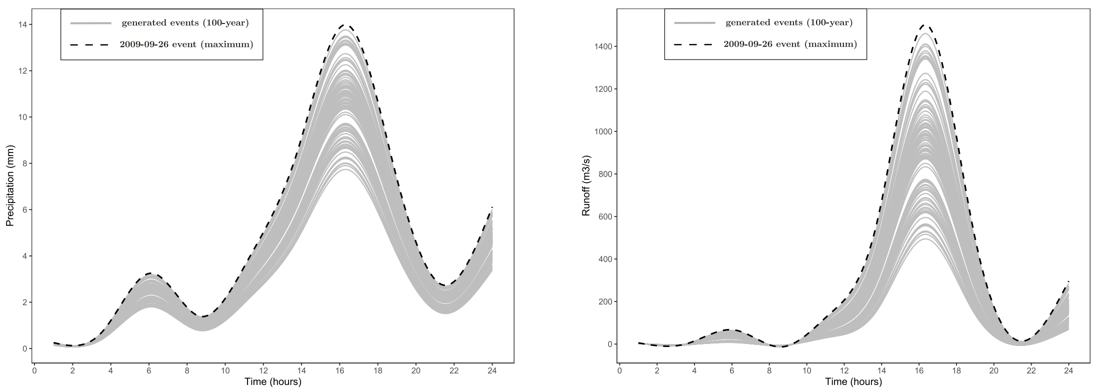

(a) (b)

Figure 18: Hyetographs (a) of generated EPEs (100-year) at Oued Martil valley and their corresponding hydrographs (b). The daily precipitation is temporally disaggregated using the extreme weather event from September 26, 2009, which produced the maximum precipitation in Oued Martil valley, represented by a dashed line.

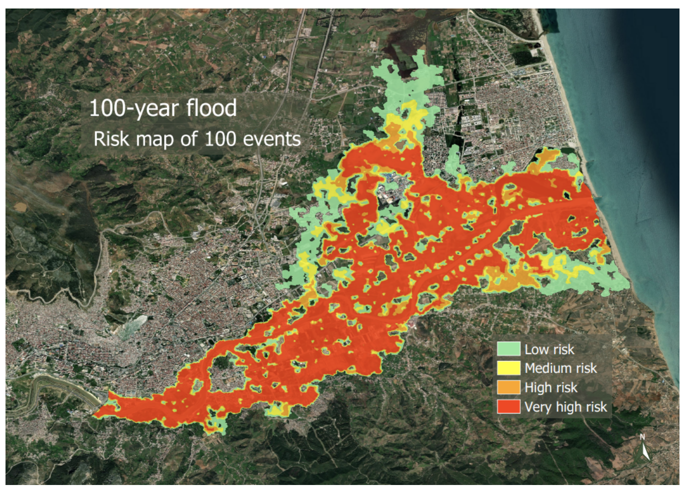

Figure 19: Same as Figure 17 but using classical Monte Carlo simulations.

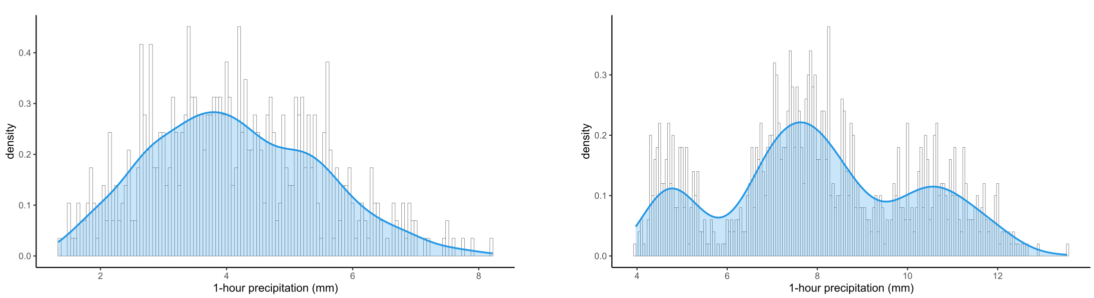

(a) (b)

Figure 20: Distribution of maximum daily precipitation calculated for 1000 EPEs generated by (a) conventional Monte Carlo simulations and (b) ExGAN simulations obtained by conditioning the model using the Regional Extremeness Measure.

rainfall-duration-frequency relationship, as investigated in (Bell, 1969). These features are widely adopted in methods prominently in various flood risk mapping analyses, as evidenced by studies such as (Aronica et al., 2012; Neal et al., 2013; Jang and Chang, 2022). Following the established protocol, a flood risk map is formulated using this classical methodology as depicted in Figure 19. It is evident that a notable disparity emerges between the risk estimates derived through this classical methodology and the approach developed herein. The hydrodynamic response, contingent upon different forcings, transitions between distinct precipitation patterns, thereby potentially impacting the overall risk assessment. However, the classical methodology which is anchored in the rainfall-duration-frequency approach, fails to consider all modes of temporal variability in EPEs (see Figure 20.a), leading to an exaggerated estimation of flood risk across significant regions. This discrepancy underscores the importance of accounting for temporal dynamics in extreme precipitation when delineating flood risk, a consideration effectively addressed in the methodology developed through ExGAN. By integrating temporal changes in extreme precipitation (see Figure 20.b), the ExGAN-based approach offers a more nuanced and accurate portrayal of flood risk across the studied region. This emphasizes the suitability of the proposed method for flood risk mapping in regions with limited data availability. In such areas, only a few historical extreme precipitation records are accessible. Note that when standard weather generators (WG) are applied to this data, the generated scenarios often fail to capture the potential complexity of precipitation processes. In contrast, the suggested methodology incorporates all complex patterns. As illustrated in Figure 20, the probability distribution of maximum hourly rainfall demonstrates the ability of the proposed methodology to capture the complexity of extreme precipitation events. Unlike the classical Monte-Carlo simulation, which produces a unimodal distribution, the suggested approach reveals a multimodal distribution, highlighting its effectiveness in representing diverse precipitation patterns. This explains also why the standard WGs overestimate the flood risk compared to the proposed methodology.

4 Conclusions

There exist diverse methodologies for producing flood risk maps, yet those grounded in hydrodynamics modeling hold significant appeal owing to their physical-based nature, particularly when adopting probabilistic approaches. However, the creation of flood maps is inherently challenged by a spectrum of uncertainties, spanning from epistemic to aleatoric sources. Notably, generating synthetic precipitation scenarios that accurately capture extreme statistics while reflecting the regional climate has historically presented a significant hurdle within this domain. In our current study, we leverage generative machine learning techniques, specifically an ExGAN model, to address this challenge by generating highly reliable synthetic extreme precipitation scenarios. Subsequently, through temporal disaggregation, these patterns of the synthetic extreme precipitation are propagated across the domain. Our results underscore the capability of the proposed model to replicate diverse forms of extreme precipitation patterns accurately. Additionally, these models can be tailored to specific probability thresholds, thereby defining distinct return periods for each generated precipitation scenario. Employing these synthetic precipitation scenarios as a driving parameter within a simplified hydrological model, we estimate runoff for each scenario. This runoff data serves as foundational input for a meticulously calibrated hydrodynamics model. Our methodology underwent rigorous testing in a highly vulnerable Mediterranean area in northern Morocco, specifically focusing on the Martil river. Validation and calibration of both the hydrological and hydrodynamical models were conducted using historical flooding data from March 2021. Subsequent to model calibration, we generated various extreme precipitation scenarios aligned with the local climatology. For each scenario, the corresponding hydrodynamics were evaluated, facilitating the creation of flood risk maps for two distinct return periods (50 and 100 years). Our findings indicate that increasing the return period extends the areas at risk more than intensifying the risk itself. Moreover, two different methods of training ExGAN were adopted here, namely Local Extremeness Measure and Regional Extremeness Measure. We demonstrate that training the models with regional information improve the accuracy of the risk estimation. Comparison with classical Monte Carlo sampling strategies for probabilistic flood mapping revealed a substantial overestimation of risk in the latter methodology. It is crucial to note that while uncertainties stemming from the sampling strategy contribute significantly to hydrodynamic models, other pertinent parameters must also be carefully considered, a focus of our forthcoming studies. In fact, a significant portion of flood risk maps relies on hydrological and hydrodynamical models which are susceptible to uncertainty stemming from various sources. Therefore, it is crucial to address these uncertainties effectively to establish a level of confidence associated with the risk maps. Furthermore, the ability of ExGAN to train extreme precipitation patterns from observed data presents a promising avenue, particularly in addressing climate change impacts. Needless to mention that by capturing shifts in extreme precipitation patterns, this strategy mitigates potential discrepancies between historical and future climatic patterns, thereby offering a solution to a longstanding challenge in statistical methods employed for assessing climate change impacts on flood risk mapping.

The results presented in this study offer several advantages for flood risk mapping. Firstly, the use of ExGAN allows for the consideration of various modes of extreme precipitation variability, unlike standard methods that rely on single events, which can lead to overestimation of risk. Secondly, the utilization of carefully selected gridded data, in contrast to rain gauge data, enables the incorporation of spatial variability in extreme precipitation, thereby improving the reliability of flood risk mapping. Another compelling advantage of using open gridded data is the ability to conduct such analyses even in vulnerable regions with limited data availability. Furthermore, following effective training of ExGAN, as demonstrated in the results, multiple scenarios of realistic extreme precipitation patterns can be generated, overcoming the limitations of classical methodologies. From a practical standpoint, accurate flood risk mapping, such as that presented in this study, facilitates informed decision-making, enhances the effectiveness of response measures, and contributes to improved public safety and reduced loss of life and property during flood events. Moreover, accurate flood risk mapping aids insurers in determining appropriate premiums and coverage limits, thereby reducing financial losses associated with flood-related claims. Additionally, homeowners and businesses can make informed decisions regarding property investment and risk management based on flood risk maps. Furthermore, flood risk mapping has implications for environmental conservation efforts. By identifying flood-prone areas and natural floodplains, policymakers can prioritize the conservation and restoration of ecosystems that provide valuable flood regulation services. Protecting these natural features can help mitigate flood risks, enhance biodiversity, and safeguard ecosystem services.

Author contributions

RB and AC collected and analyzed the data, performed simulations, contributed to the interpretation of results and drafted the initial manuscript. NY participated in the data acquisition and contributed to the final approval of the version to be published. MS supervised the research, and contributed to the methodology. NEM conceived and designed the study, supervised the research and contributed to the methodology. All authors contributed substantially to the conception and design of the work, revised it critically for important intellectual content, and approved the final version for publication.

Acknowledgments and funding

The work carried out by RB was supported financially by the MICODIR project, funded by the APRD Program. Thus, we extend our gratitude to the Moroccan Ministry of Higher Education, Scientific Research, and Innovation, as well as the OCP Foundation.

AC's work was funded by the UMRP project, supported financially by OCP. Additionally, our appreciation goes to the Tanger-Tetouan-AlHoceima region for funding the SYNOPCE-TTA project and aiding in data acquisition. The authors extend their gratitude to Prof. Rachid Ababou for engaging in insightful discussions. Additionally, the valuable comments provided by the reviewer and editor have significantly enhanced the quality of this study. Their contributions are sincerely appreciated.

Data availability

ERA5 reanalysis data are available at https://doi.org/10.24381/cds.adbb2d47. The data employed for calibrating the model cannot be publicly shared however, it is available upon reasonable request to the corresponding author.

Appendix A: Algorithm used in the present study.

Algorithm A. 1 : 24-hour event generation

Input: let

$RR.days$ = ERA5 daily precipitation

$RR.hours$ = ERA5 hourly precipitation

$threshold$ = 99th percentile of wet days ($RR.days > 1mm/day$)

N = Number of events to generate

Algorithm:

Set $genEVs$ as empty list

for i in $1 : N$ **do** ▷ Generate N daily rainfall events using ExGAN

  $genEVs = concatenate(genEVs, ExGAN(RR.days))$

end for

$realEVs$ = days for $RR.days$ with total precipitation $> threshold$

Set $genEVs.hours$ as empty list

for $genEV$ in $genEVs$ **do** ▷ Identify the closest event among $realEVs$ to $genEV$

  $realEV = closest(genEV, realEVs)$

  $realEV.hours$ = hourly distribution of $realEV$ (from $RR.hours$)

  ▷ Compute the hourly distribution of $genEV$

  $genEV.hours = (realEV.hours/realEV) * genEV$

  $genEVs.hours = concatenate(genEVs.hours, genEV.hours)$

end for

Output:

$genEVs.hours$ = hourly total precipitation for the N generated events

Related function:

closest(genEV, realEVs):

1: Identify the 5 first events that maximize the total number of common pixels (pixels with precipitation >1mm) between $genEV$ and each of $realEVs$

2: From the 5 events chose the one that minimizes the total difference between $genEV$ and each of the 5 events

References

Aggarwal, A., M. Mittal, and G. Battineni, 2021: Generative adversarial network: An overview of theory and applications. *International Journal of Information Management Data Insights*, **1 (1)**, 100 004, URL https://doi.org/10.1016/j.jjimei.2020.100004.

Al-Ghosoun, A., N. El Moçayd, and M. Seaid, 2021: A surrogate model for efficient quantification of uncertainties in multilayer shallow water flows. *Environmental Modelling & Software*, **144**, 105 176.

Apel, H., A. H. Thieken, B. Merz, and G. Blöschl, 2004: Flood risk assessment and associated uncertainty. *Natural Hazards and Earth System Sciences*, **4 (2)**, 295–308.

Aronica, G., F. Franza, P. Bates, and J. Neal, 2012: Probabilistic evaluation of flood hazard in urban areas using monte carlo simulation. *Hydrological Processes*, **26 (26)**, 3962–3972.

Ballesteros-Cánovas, J., B. Czajka, K. Janecka, M. Lempa, R. Kaczka, and M. Stoffel, 2015: Flash floods in the tatra mountain streams: Frequency and triggers. *Science of the Total Environment*, **511**, 639–648.

Bárdossy, A., and G. Pegram, 2009: Copula based multisite model for daily precipitation simulation. *Hydrology and Earth System Sciences*, **13 (12)**, 2299–2314.

Barton, A. J., 2019: Blue kenue enhancements from 2014 to 2019. *XXVIth TELEMAC-MASCARET User Conference, 15th to 17th October 2019, Toulouse.*

Bell, F. C., 1969: Generalized rainfall-duration-frequency relationships. *Journal of the hydraulics division*, **95 (1)**, 311–328.

Besombes, C., O. Pannekoucke, C. Lapeyre, B. Sanderson, and O. Thual, 2021: Producing realistic climate data with generative adversarial networks. *Nonlinear Processes in Geophysics*, **28 (3)**, 347–370.

Bhatia, S., A. Jain, and B. Hooi, 2021: Exgan: Adversarial generation of extreme samples. *Proceedings of the AAAI Conference on Artificial Intelligence*, Vol. 35, 6750–6758, URL https://doi.org/10.1609/aaai.v35i8.16834.

Boulaguiem, Y., J. Zscheischler, E. Vignotto, K. van der Wiel, and S. Engelke, 2022: Modeling and simulating spatial extremes by combining extreme value theory with generative adversarial networks. *Environmental Data Science*, **1**, e5, URL https://doi.org/10.1017/eds.2022.4.

Chaqdid, A., A. Tuel, A. El Fatimy, and N. El Moçayd, 2023: Extreme rainfall events in morocco: Spatial dependence and climate drivers. *Weather and climate extremes*, **40**, 100 556, URL https://doi.org/10.1016/j.wace.2023.100556.

Cowpertwait, P., C. Kilsby, and P. O'Connell, 2002: A space-time neyman-scott model of rainfall: Empirical analysis of extremes. *Water Resources Research*, **38 (8)**, 6–1.

Dash, P., and J. Sar, 2020: Identification and validation of potential flood hazard area using gis-based multi-criteria analysis and satellite data-derived water index. *Journal of Flood Risk Management*, **13 (3)**, e12 620.

El Moçayd, N., S. Kang, and E. A. B. Eltahir, 2020: Climate change impacts on the water highway project in morocco. *Hydrology and Earth System Sciences*, **24 (3)**, 1467–1483, doi:10.5194/hess-24-1467-2020, URL https://hess.copernicus.org/articles/24/1467/2020/.

Gai, L., J. Baartman, M. Mendoza-Carranza, F. Wang, C. Ritsema, and V. Geissen, 2018: A framework approach for unravelling the impact of multiple factors influencing flooding. *Journal of Flood Risk Management*, **11 (2)**, 111–126.

Hawkins, R. H., R. Jiang, D. Woodward, A. Hjelmfelt, J. Van Mullem, and Q. Quan, 2002: Runoff curve number method: examination of the initial abstraction ratio. *Proceedings of the Second Federal Interagency Hydrologic Modeling Conference*, Las Vegas, Nevada. US Geological Survey, Vol. 28, URL https://doi.org/10.1061/40685(2003)30.

Hersbach, H., and Coauthors, 2020: The ERA5 global reanalysis. *Quarterly Journal of the Royal Meteorological Society*, **146 (730)**, 1999–2049, URL https://doi.org/10.1002/qj.3803.

Hervouet, J.-M., 2007: *Hydrodynamics of free surface flows : modelling with the finite element method*. Wiley, 341 pp., URL https://onlinelibrary.wiley.com/doi/book/10.1002/9780470319628.

Hughes, J. P., P. Guttorp, and S. P. Charles, 1999: A non-homogeneous hidden markov model for precipitation occurrence. *Journal of the Royal Statistical Society Series C: Applied Statistics*, **48 (1)**, 15–30.

Huster, T., J. Cohen, Z. Lin, K. Chan, C. Kamhoua, N. O. Leslie, C.-Y. J. Chiang, and V. Sekar, 2021: Pareto gan: Extending the representational power of gans to heavy-tailed distributions. *International Conference on Machine Learning*, PMLR, 4523–4532.

Jang, J.-H., and T.-H. Chang, 2022: Flood risk estimation under the compound influence of rainfall and tide. *Journal of Hydrology*, **606**, 127 446.

Karrouchi, M., M. O. Touhami, M. Oujidi, and M. Chourak, 2016: Cartographie des zones à risque d'inondation dans la région tanger-tétouan: Cas du bassin versant de martil (nord du maroc)/[mapping of flooding risk areas in the tangier-tetouan region: Case of martil watershed (northern morocco)]. *International Journal of Innovation and Applied Studies*, **14 (4)**, 1019.

Khattabi, A. E., 2021: Reproduction d'anatidés rares dans le delta de l'oued martil, au nord du maroc. **18**, 55–62.

Koutsoyiannis, D., A. Paschalis, and N. Theodoratos, 2011: Two-dimensional hurst–kolmogorov process and its application to rainfall fields. *Journal of Hydrology*, **398 (1-2)**, 91–100.

Li, G., X. Wu, J.-C. Han, B. Li, Y. Huang, and Y. Wang, 2023: Flood risk assessment by using an interpretative structural modeling based bayesian network approach (ism-bn): An urban-level analysis of shenzhen, china. *Journal of Environmental Management*, **329**, 117 040.

Mora, C., and Coauthors, 2018: Broad threat to humanity from cumulative climate hazards intensified by greenhouse gas emissions. *Nature climate change*, **8 (12)**, 1062–1071.

Neal, J., C. Keef, P. Bates, K. Beven, and D. Leedal, 2013: Probabilistic flood risk mapping including spatial dependence. *Hydrological Processes*, **27 (9)**, 1349–1363, doi:https://doi.org/10.1002/hyp.9572, https://onlinelibrary.wiley.com/doi/pdf/10.1002/hyp.9572.

Nguyen, L., D. Tri, T. Thai, and N. C. Don, 2018: Application of a two-dimensional model for flooding and floodplain simulation: Case study in tra khuc-song ve river in viet nam. *Lowland Technology International*, **20**, 367–378.

Paschalis, A., P. Molnar, S. Fatichi, and P. Burlando, 2013: A stochastic model for high-resolution space-time precipitation simulation. *Water Resources Research*, **49 (12)**, 8400–8417.

Prokos, H., H. Baba, D. Lóczy, and Y. El Kharim, 2016: Geomorphological hazards in a mediterranean mountain environment - example of tétouan, morocco. *Hungarian Geographical Bulletin*, **65**, 283–295, doi:10.15201/hungeobull.65.3.6.

Racsko, P., L. Szeidl, and M. Semenov, 1991: A serial approach to local stochastic weather models. *Ecological modelling*, **57 (1-2)**, 27–41.

Radwan, F., A. Alazba, and A. Mossad, 2019: Flood risk assessment and mapping using ahp in arid and semiarid regions. *Acta Geophysica*, **67**, 215–229.

Ramanathan, A., P.-A. Versini, D. Schertzer, R. Perrin, L. Sindt, and I. Tchiguirinskaia, 2022: Stochastic simulation of reference rainfall scenarios for hydrological applications using a universal multi-fractal approach. *Hydrology and Earth System Sciences*, **26 (24)**, 6477–6491.

Rian, M., 2021: Integrated assessment of ecological and urban implementation of martil river in north morocco. M.S. thesis, Altınbaş Üniversitesi.

Richardson, C. W., 1981: Stochastic simulation of daily precipitation, temperature, and solar radiation. *Water resources research*, **17 (1)**, 182–190.

Roy, P. T., N. El Moçayd, S. Ricci, J.-C. Jouhaud, N. Goutal, M. De Lozzo, and M. C. Rochoux, 2018: Comparison of polynomial chaos and gaussian process surrogates for uncertainty quantification and correlation estimation of spatially distributed open-channel steady flows. *Stochastic environmental research and risk assessment*, **32**, 1723–1741.

Satour, N., B. Benyacoub, N. El Moçayd, Z. Ennaimani, S. Niazi, N. Kassou, and I. Kacimi, 2023: Machine learning enhances flood resilience measurement in a coastal area–case study of morocco. *Journal of Environmental Informatics*, **42 (1)**.

Satour, N., O. Raji, N. El Moçayd, I. Kacimi, and N. Kassou, 2021: Spatialized flood resilience measurement in rapidly urbanized coastal areas with a complex semi-arid environment in northern morocco. *Natural Hazards and Earth System Sciences*, **21 (3)**, 1101–1118, URL https://nhess.copernicus.org/articles/21/1101/2021/.

Schertzer, D., and S. Lovejoy, 1987: Physical modeling and analysis of rain and clouds by anisotropic scaling multiplicative processes. *Journal of Geophysical Research: Atmospheres*, **92 (D8)**, 9693–9714.

SCS, 1972: *National engineering handbook*, Vol. Supplement A, Section 4, Chapter 10. Soil Conservation Service, USDA, Washington.

Semenov, M. A., R. J. Brooks, E. M. Barrow, and C. W. Richardson, 1998: Comparison of the wgen and lars-wg stochastic weather generators for diverse climates. *Climate research*, **10 (2)**, 95–107.

Shadeed, S., 2023: The potential use of the scs-cn method to estimate extreme floods in the west bank data-scarce catchments. *An-Najah University Journal for Research, A: Natural Sciences*, **37 (2)**.

Singh, P., S. K. Mishra, R. Berndtsson, M. K. Jain, and R. Pandey, 2015: Development of a modified sma based mscs-cn model for runoff estimation. *Water resources management*, **29**, 4111–4127.

Soulis, K. X., and J. Valiantzas, 2012: Scs-cn parameter determination using rainfall-runoff data in heterogeneous watersheds–the two-cn system approach. *Hydrology and Earth System Sciences*, **16 (3)**, 1001–1015.

Szegedy, C., V. Vanhoucke, S. Ioffe, J. Shlens, and Z. Wojna, 2016: Rethinking the inception architecture for computer vision. *Proceedings of the IEEE conference on computer vision and pattern recognition*, 2818–2826.

Tuel, A., and N. El Moçayd, 2023: Evaluating extreme precipitation in gridded datasets with a novel station database in morocco. *Stochastic Environmental Research and Risk Assessment*, **37 (8)**, 3085–3097.

Tung, V., P. Nguyen, L. Chua, and A. Law, 2015: Two-dimensional hydrodynamic modelling of flood inundation for a part of the mekong river with telemac-2d. *British*

Journal of Environment and Climate Change, **5**, 162–175, doi:10.9734/BJECC/2015/12885.

Ullrich, S. L., M. Hegnauer, D. V. Nguyen, B. Merz, J. Kwadijk, and S. Vorogushyn, 2021: Comparative evaluation of two types of stochastic weather generators for synthetic precipitation in the rhine basin. *Journal of Hydrology*, **601**, 126 544.